materials

MDPI

Article

Review on the Use of Superconducting Bulks for Magnetic Screening in Electrical Machines for Aircraft Applications

Rémi Dorget [1,2,†], Quentin Nouailhetas [1,3,*,†], Alexandre Colle [4], Kévin Berger [1], Kimiaki Sudo [5], Sabrina Ayat [2], Jean Lévêque [1], Michael Rudolf Koblischka [3,5], Naomichi Sakai [5], Tetsuo Oka [5] and Bruno Douine [1]

1 Groupe de Recherche en Energie Electrique de Nancy, Université de Lorraine, GREEN, 54000 Nancy, France; remi.dorget@univ-lorraine.fr (R.D.); kevin.berger@univ-lorraine.fr (K.B.); jean.leveque@univ-lorraine.fr (J.L.); bruno.douine@univ-lorraine.fr (B.D.)
2 Safran Tech, Electrical & Electronic Systems Research Group, Rue des Jeunes Bois, Châteaufort, 78114 Magny-Les-Hameaux, France; sabrina.ayat@safrangroup.com
3 Experimentalphysik, Saarland University, P.O. Box 151150, 66041 Saarbrücken, Germany; m.koblischka@gmail.com
4 Airbus UpNext, 31300 Toulouse, France; alexandrecolle57@gmail.com
5 Shibaura Institute of Technology, Tokyo 135-8548, Japan; ac16052@shibaura-it.ac.jp (K.S.); nsakai@shibaura-it.ac.jp (N.S.); superoka49@gmail.com (T.O.)
* Correspondence: quentin.nouailhetas@univ-lorraine.fr
† These authors contributed equally to this work.

Abstract: High-Temperature Superconductors (HTS) considerably accelerate the development of superconducting machines for electrical engineering applications such as fully electrical aircraft. This present contribution is an overview of different superconducting materials that can be used as magnetic screens for the inductor of high specific power electrical machines. The impact of the material properties, such as the critical temperature (T_c) and the critical current density (J_c), on the machine performances is evaluated. In addition, the relevance to flux modulation machines of different HTS bulk synthesis methods are addressed.

Keywords: superconducting bulk; superconducting electrical machine; flux modulation machine

Citation: Dorget, R.; Nouailhetas, Q.; Colle, A.; Berger, K.; Sudo, K.; Ayat, S.; Lêvêque, J.; Koblischka, M.R.; Sakai, N.; Oka, T.; et al. Review on the Use of Superconducting Bulks for Magnetic Screening in Electrical Machines for Aircraft Applications. *Materials* **2021**, *14*, 2847. https://doi.org/10.3390/ma14112847

Academic Editor: Israel Felner

Received: 29 April 2021
Accepted: 23 May 2021
Published: 26 May 2021

1. Introduction

The development of High-Temperature Superconductors (HTSs) such as the cuprate family with the REBaCuO superconductors (Rare Earth elements (RE)), the Iron-Based Superconductors (IBS) with the Pnitide and Chalcogen families and the MgB_2 compound allow a quick evolution of superconducting devices for many applications. Among them, lead by ecological, economical, and practical needs, the electrical machines associated with superconducting materials such as electromagnet [1], permanent magnets [2–5], or windings [6,7] look increasingly more attractive for future transports such as electrical ships [8], aircraft [9–11], and levitation trains [12] for the high specific power potential of HTS machines. Indeed, for the aviation sector in particular, the growing need for electrical power on board requires the development of electrical machines with a target power-to-weight ratio of 20 kW/kg for MW class machines [4,13,14].

Several topologies of HTS synchronous machines are considered promising such as rotor-wound machines [15,16]; superconducting "permanent magnet" machines, made from HTS bulks [17] or HTS stacks of tapes [18]; and flux modulation machines [19–23]. The last topology, as illustrated in Figure 1 in its axial flux version, is composed by a static solenoid coil made of superconducting tapes which produce a DC magnetic field. The second element of the inductor consists of superconducting bulks located on the rotor; these pellets are used in the mixed state, thus the application of the coil magnetic field will induce currents in the material, which will screen the coil field. The flux density

behind the bulks is therefore reduced, and there is a magnetic flux modulation in the air gap. Eventually, this variations will induce an electromotive force in the three phase windings located on both sides of the rotor. This topology does not requires any slip rings contrary to rotor-wound machines and the magnetization can be controlled, unlike superconducting "permanent magnet" machines while showing promising performances. Indeed, flux modulations machines reach high specific powers by having a large magnetic field in the air gap (>2 T), whereas conventional machine are limited by the iron magnetic saturation. Thus, it is possible to reach high power to mass ratio without increasing the rotational speed. In contrast to aircraft conventional machines, which tend to increase in speed and require the use of a mechanical gearbox [24], the expected operating speed for flux modulation motors is only a few thousand rpm.

In order to properly screen a large magnetic field, the material used for the rotor must be a efficient superconductor. Furthermore, as liquid hydrogen is likely to become the main coolant for aircraft applications [11], the working temperature of the machine must be approximately 20 K. Therefore, to ensure a comfortable margin, a critical temperature T_c above 30 K is needed for the potential candidates.

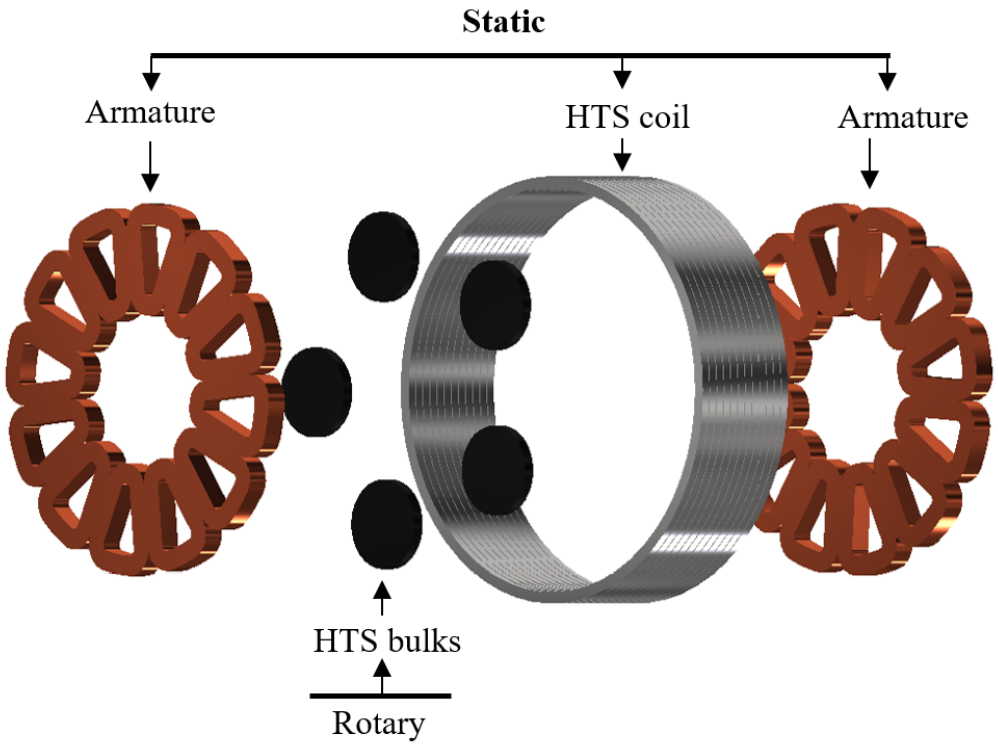

Figure 1. Exploded view of an axial flux modulation machine's active components. Static parts: two copper armatures and one High-Temperature Superconductor (HTS) coil. Rotating parts: a set of HTS bulks.

Along this paper, we will analyze and evaluate the performance as well as the relevancy of the following bulk superconducting materials for use in a reliable industrial flux modulation machine for aircraft applications:

- The Pnictide and Chalcogen families of Iron-based superconductors (IBS) [25–28] with T_c as high as 46 K for the NaFeSe [29,30] and 56 K for the $Sr_{0.5}Sm_{0.5}FeAsF$ [31] compound. The IBS also show very high critical magnetic field (H_{c2}) [32] and promising critical current density (J_c) at liquid hydrogen temperature [33].
- The REBaCuO materials [34] with the so-called YBaCuO [35] and GdBaCuO [36], which are the most widely used for electrical engineering applications because of their really high superconducting properties [37,38].

- The MgB_2 compound [39] with a T_c of 39 K, an acceptable H_{c2} and a very high J_c [40,41] has a good potential as trapped field permanent magnet [42,43].

The required superconducting properties, i.e., the critical current density J_c, for that type of machine will be determined using simulation tools in a first section. In a second section, the existing synthesis and preparation techniques for each materials and their relevancy for custom and mass production will be highlighted.

2. Critical Current Density and Magnetic Shielding Properties

Naturally, the critical current density J_c of HTS materials has an impact on a flux modulation machine performances. To study the J_c influence on the flux modulation quality, we made a numerical 2D axisymetric model of the bulk using the commercial software COMSOL Multiphysics. The parameter values of this model are listed in the Table 1. The Maxwell equations are expressed by the **H**-formulation linking the single component of the electric field along the θ-direction $E_\theta(r,z)$ and the two components of the magnetic field along the r and z directions $H_r(r,z)$ and $H_z(r,z)$, respectively:

$$\mu_0 \frac{\partial H_r(r,z)}{\partial t} - \frac{\partial E_\theta(r,z)}{\partial z} = 0 \tag{1}$$

$$\mu_0 \frac{\partial H_z(r,z)}{\partial t} + \frac{\partial E_\theta(r,z)}{\partial r} + \frac{E_\theta(r,z)}{r} = 0 \tag{2}$$

The magnetic field is linked to the current density single component $J_\theta(r,z)$ through the Maxwell–Ampere equation:

$$J_\theta(r,z) = \frac{\partial H_r(r,z)}{\partial z} - \frac{\partial H_z(r,z)}{\partial r} \tag{3}$$

The electromagnetic behavior of the bulk is modeled through an $E-J$ law with a constant J_c [44]:

$$E_\theta(r,z) = \frac{E_c}{J_c} \left(\frac{|| J_\theta(r,z) ||}{J_c} \right)^{n-1} J_\theta(r,z) \tag{4}$$

Table 1. Geometrical and physical parameters of the 2-D asymmetric simulation of the bulk on COMSOL.

Symbol	Parameter	Value
E_c	Critical electric field	1 μV/cm
n	index of the power law	20
R	Bulk radius	40 mm
h	Bulk thickness	10 mm
$\mu_0 H_a$	Applied magnetic field	0–4 T

The magnetic field applied by the coil is modeled as an homogeneous magnetic field applied in the z-direction. The simulation is time-dependent and consists of two steps: First, the applied field ramp rise from 0 T to the desired value $\mu_0 H_a$ in 100 s. The applied field is then kept constant for 100 s to reach the steady state at which the the flux modulation is observed 3 mm behind the bulk. Eventually, we evaluate the performances by calculating the amplitude of the first space harmonic of the field variation B_1, which is proportional to the torque produced in an electrical machine and is calculated from

$$B_1 = \frac{1}{R} \int_0^{2R} \mu_0 H_z(r, \frac{h}{2} + 3 \text{ mm}) \cos\left(\frac{2\pi r}{4R}\right) dr \tag{5}$$

Figure 2 shows the variation of B_1 versus the J_c for different values of applied magnetic field. Although the critical current density has a clear influence on the machine power, one can observe that above a certain threshold, the flux modulation amplitude does not increase anymore. Thus, a bulk with a critical current equal to 2000 A/mm^2 will provide performances close to a perfectly diamagnetic bulk which corresponds to an infinite critical current.

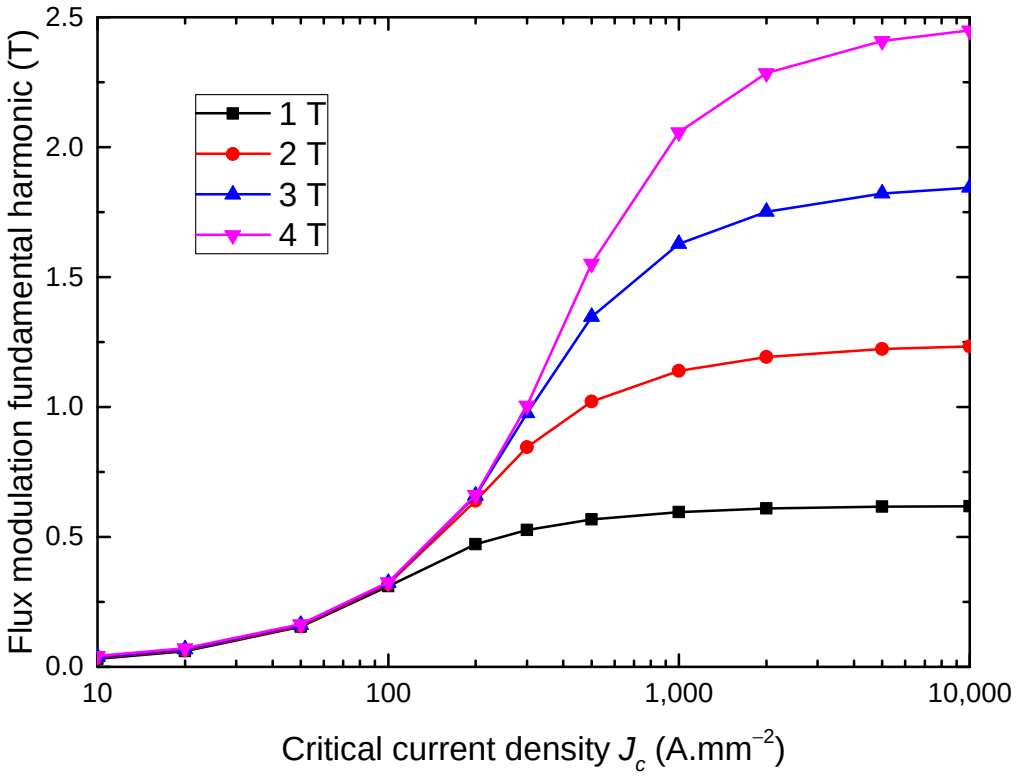

Figure 2. Simulation of the amplitude of the flux modulation fundamental harmonic in the air gap versus the bulk critical current density for applied magnetic fields of 1, 2, 3, and 4 T. The machine torque is proportional to the first harmonic of the air gap magnetic field.

To properly understand this last result, one must analyze the behavior of the magnetic field and current in the bulk while subjected to the coil field. Figure 3 shows the 3-D current distribution in the bulk while subjected to 3 T for J_c equal to 500 A/mm^2 and 2000 A/mm^2. It can be seen that the current is penetrating the bulk deeply at 500 A/mm^2 while remaining close to the surface above 2000 A/mm^2. As shown on Figure 4, the parts of the bulks penetrated by the current are those where the field is not properly screened. Therefore, increasing J_c will decrease the penetration depth of the bulk, which explains the strong gains in performance when going from complete penetration to a case where the current only flows at the extremities. However, above 2000 A/mm^2, the zero current zone does not expand much more, which limits the power increase. Based on these explanations, the curves on Figure 2 can be divided into three zones:

Below 100 A/mm^2, the applied field does not have any impact on the torque as every curves are merged because the bulk is completely penetrated by the magnetic field and provides the same modulation.

Between 100 A/mm^2 and few thousands of A/mm^2 the bulk are transitioning from complete penetration to a situation where only the edges have current flowing through them.

Eventually, above a certain applied field, the bulks move towards the asymptote of the perfectly diamagnetic bulk. In the two first zones, the machine torque is strongly linked to the bulk critical current while linked only to the applied field in the third zone.

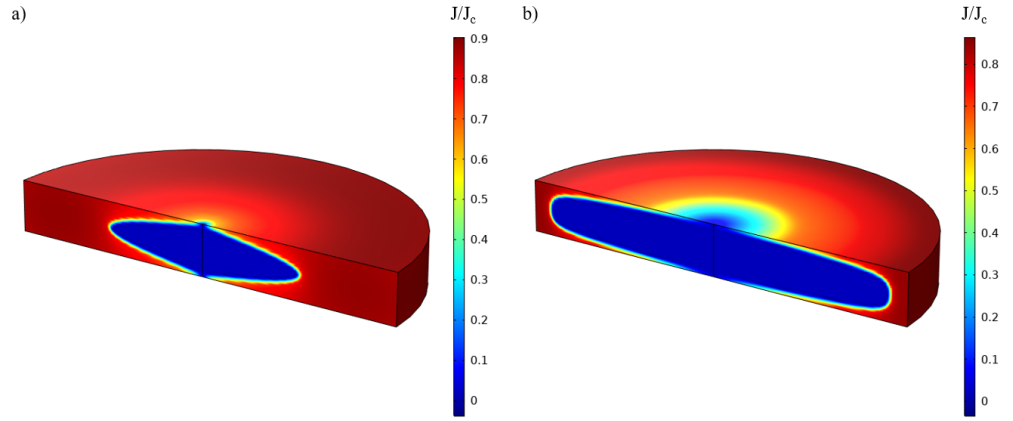

Figure 3. Ratio of current distribution to critical current in a bulk subjected to an applied field of 3 T for (**a**) $J_c = 500$ A/mm^2 and (**b**) $J_c = 2000$ A/mm^2 simulated using Comsol Multiphysics.

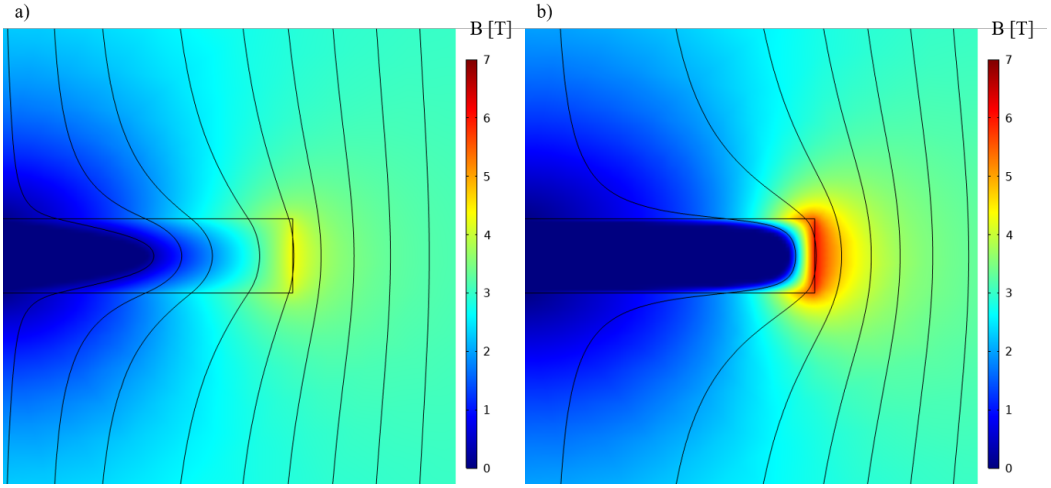

Figure 4. Modulation of the applied magnetic field by the bulk for (**a**) $J_c = 500$ A/mm^2 and (**b**) $J_c = 2000$ A/mm^2 simulated using Comsol Multiphysics.

Based on the results of these simulations, we can conclude that even though the J_c has an important impact on the performances, it is not necessarily useful to try to go beyond few thousands of A/mm^2. As the threshold above which the bulk has a behavior close to a perfect diamagnetic material depends on the applied magnetic field, we can define a modulation quality factor F_Q as the ratio of B_1 for a given J_c and B_1 for a perfect diamagnetic bulk:

$$F_Q(J_c) = \frac{B_1(J_c)}{B_1(\infty)} \tag{6}$$

Figure 5 shows the evolution of the modulation quality factor for different applied magnetic fields. If we consider a bulk as behaving as a diamagnetic material when its quality factor is above 0.95, it can be observed that 800 A/mm^2 is required for 1 T applied, while 3000 A/mm^2 is needed to properly screen 4 T.

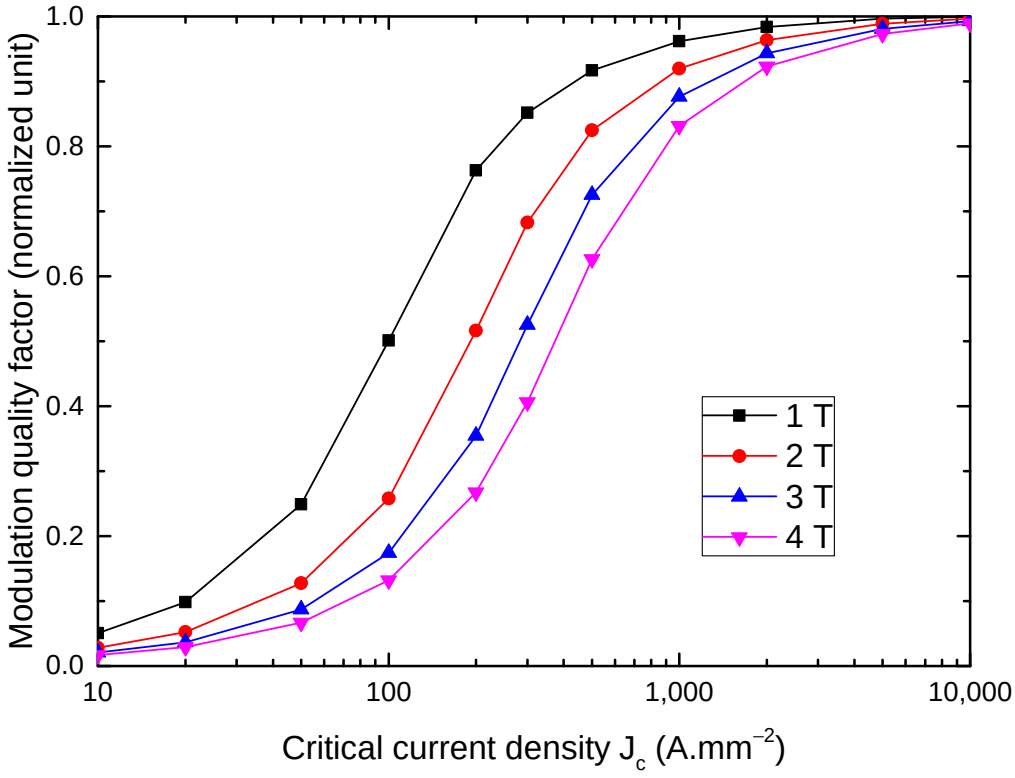

Figure 5. Simulation of the quality of the modulation versus the bulk critical current density for applied fields of 1, 2, 3, and 4 T.

As said above, the machine power is directly linked to the modulation amplitude, itself linked to the critical current density on the edge of the bulk as well as the applied magnetic field. This highlight two essential parameters for choosing the right material to be used for the shielding. Because of different variations of the critical current density with the applied magnetic field, the screening ability of a material also changes with the applied field. In this scope, the model used previously is completed by integrating the variation of the J_c with the magnetic field in the $E - J$ law. Figure 6 presents the B_1 function of the applied magnetic field for a 80 mm in diameter disk-shaped bulk made of different superconducting materials presented in the introduction compared with a perfectly diamagnetic bulk.

As expected, the YBaCuO bulk [45] exhibits properties close to a perfect diamagnet for magnetic fields as high as 2 T due to a critical current of 4500 A/mm^2 and starts to shows a tiny difference at 4 T where the critical current reached 5000 A/mm^2. This increase of critical current is due to the well-known fishtail effect [46].

The BaKFeAs materials also shows a promising flux modulation property as, like for the YBaCuO, it is a single crystal with a critical current staying above 1000 A/mm^2 at 4 T [47] thanks to the fishtail effect. These performances needs to be confirmed for larger samples as only few mm^3 could be synthesized with the current methods [47,48].

However, for the MgB_2 [41], KFeSe [33], $Bi_2Sr_2Ca_2Cu_3O_x$ (Bi2223) [49], and CaKFeAs [50], we observe a certain value of the applied field for each material at which the B_1 is maximized, which implies that for a machine made with these materials, an increase in the HTS coil size can lead to a decrease in the magnetic loading and the machine power. This is caused by the decay of the J_c with the magnetic field. For instance, while the critical current at 0 T is approximately 500 A/mm^2 for both KFeSe and Bi2223, the J_c of Bi2223 decreases to 100 A/mm^2 at 2 T, while the KFeSe is still at 300 A/mm^2, which explains the better performance of KFeSe compared to Bi2223. Note that although it is not visible on the Figure 6, the B_1 of YBaCuO and BaKFeAs also reach a maximum but at much higher magnetic fields because of the fishtail effect. Nevertheless, as magnetic field higher than

4 T are not likely to be used in electrical machines, MgB_2 and KFeSe are still interesting options as they can provide significant flux modulations.

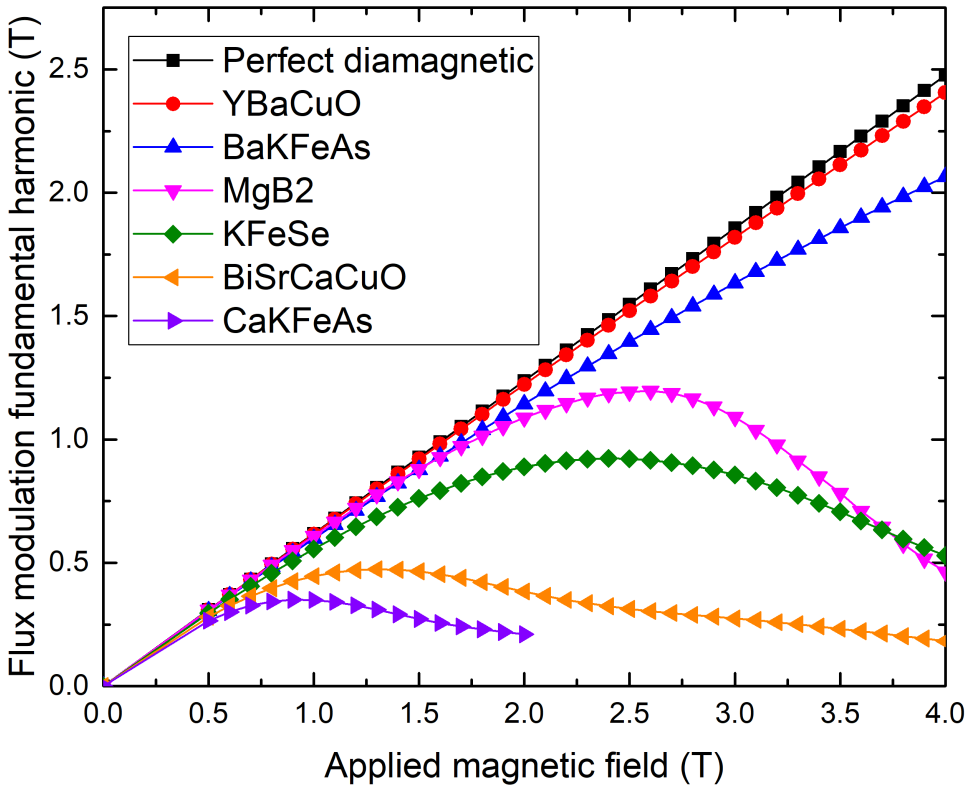

Figure 6. Simulated amplitude of the flux modulation fundamental harmonic in the air gap versus applied magnetic field for different superconducting materials. The material properties are extracted from the works in [33,41,45,47,49,50].

These measurements highlight another key parameter, which is the value of the external magnetic field generated by the superconducting coil. Where for the MgB_2 and the KFeSe this value is selected according to the optimize flux modulation, it is only limited by the capacity of generated high magnetic field with the coils in the case of the YBaCuO and the BaKFeSe materials. Indeed, producing higher magnetic fields means a bigger and so heavier superconducting coil as it is presented in Figure 7. It represents the magnetic field produced by an HTS REBaCuO coil in a flux modulation machine function of the HTS tapes mass required in a coil of 352 mm in diameter and 107 mm in length designed using a 2D asymmetric model presented in [22]. Note that generating a large magnetic field requires a heavier coil, as the critical current density of the HTS tapes decreases with the magnetic field. Thus, the ratio of the coil magnetic field and the coil weight decreases with the generated magnetic field, making the magnetic load increase for a flux modulation machine costly.

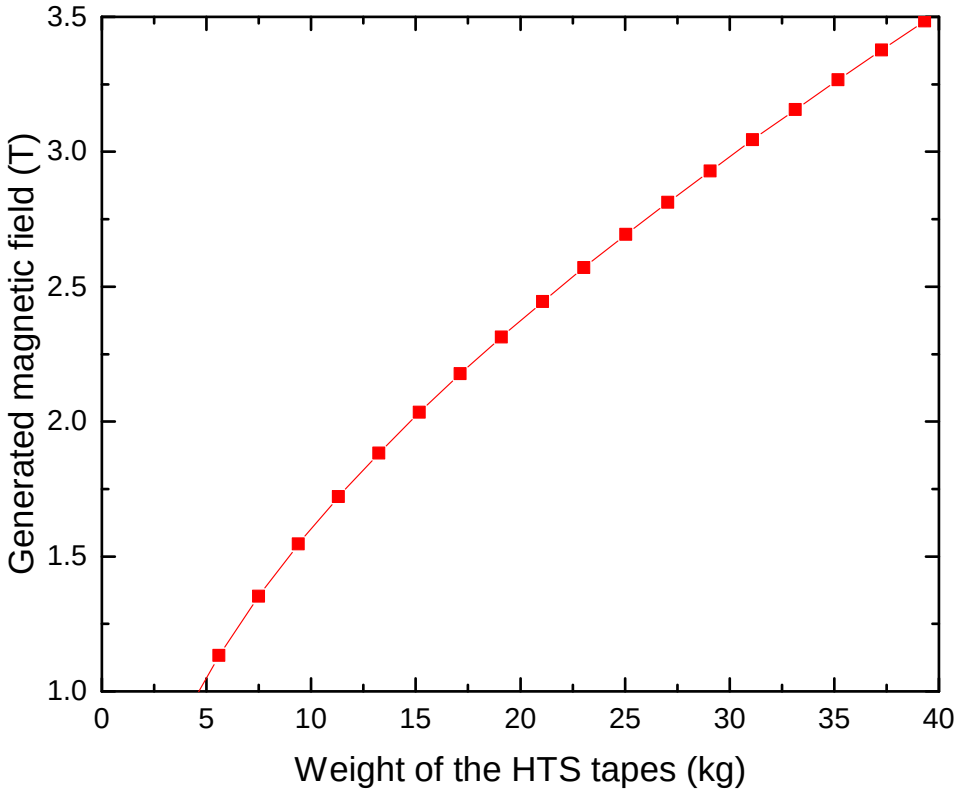

Figure 7. Simulation of the generated magnetic field at the center of a YBCO coil function of its weight for a coil of 352 mm in diameter and 107 mm in length.

3. Impact of the Synthesis Process on Performances

The most recent flux modulation prototype presented in [23] was realized using multi-seeded YBaCuO bulks. Figure 8 shows the rotor assembled with five of these bulks. The multi-seeded melt growth method (MSMG) allows creating large REBaCuO bulks in a reasonable frame of time; it has been observed, however, that the superconducting properties along the grain boundaries were inferior to the properties in the single crystals [51].

Based on the measurements realized on this prototype, two 3-D models are used to assess the grain boundaries influence on the machine performances:

- Single-Grain model (SG): A time-dependent **H**-formulation model, where the superconductors have homogeneous properties. Its critical current density is fixed to 2000 A/mm^2. This model is used as a reference and corresponds to a single-seeded bulk.
- Multi-Grain model (MG): A model considering a significant drop of the J_c at the grain boundaries of the bulk. Figure 9 shows one of the prototype's bulk with the four seeds used and the representation of the MG model with the grain boundaries regions. To simplify, the change of the critical current density is considered sinusoidal over the boundary region. The minimal J_c in the frontier is fixed at 46 A/mm^2 to best fit the measurements.

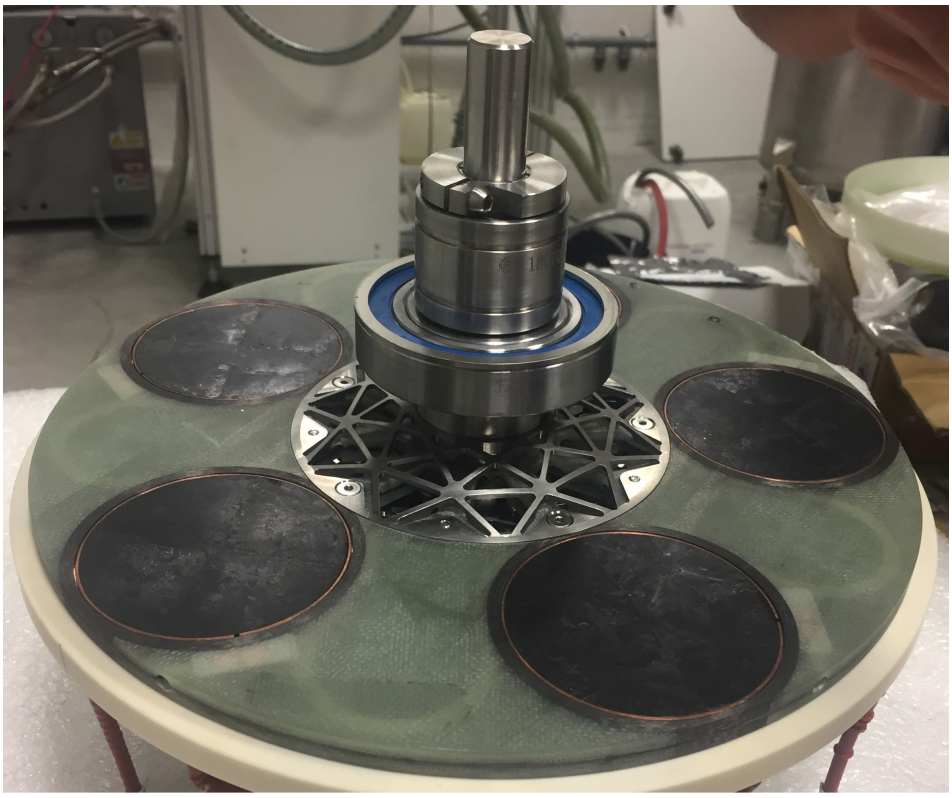

Figure 8. Superconducting rotor of the flux modulation machine prototype.

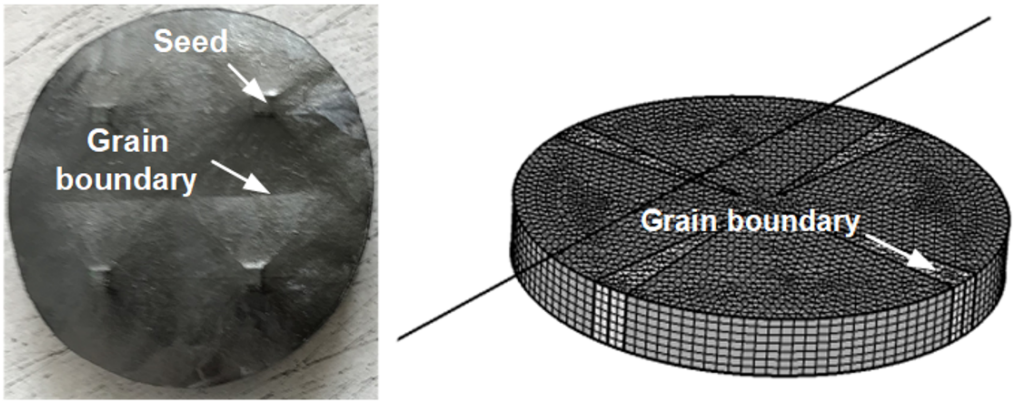

Figure 9. Left: Picture of the multi-seeded commercial bulk from ATZ of the 50 kW prototype before the polishing phase. **Right**: Geometry of the MG model considering a reduced critical current density on the grain boundaries.

For both models, a bulk with 80 mm in diameter bulk is exposed to an external magnetic flux density along the z-direction rising from 0 to 0.55 T. This latter value correspond to a current of 120 A flowing in the superconducting coil. The calculation of the flux modulation is done, on the line shown, 5 mm over the surface of the superconductor. This emplacement corresponds to the location of the Hall sensor placed out of the cryostat during the experiment.

The impact of the grain boundaries on the flux modulation can be clearly seen on the Figure 10 which shows the comparison of the SG and MG models with the measured data on the prototype. In order to have an insight of the grain boundaries influence on the machine torque, the fundamental magnetic flux density B_1 is calculated in Table 2 for each model. Thus, the torque produced with the multi-seeded bulks is 23% lower that which would have been produced with a single-seeded bulk. Additionally, as the MG

model is precise enough to predict the B_1 with a 2% error, it can be assumed that the critical current density around the grain boundaries is reduced by 98% and lead to a significant penetration of the magnetic flux in that zone.

Table 2. Comparison of the magnetic flux density fundamental value of the different models with the measured data.

Model	B_1 (T)
SG model	0.280
MG model	0.220
Measured	0.215

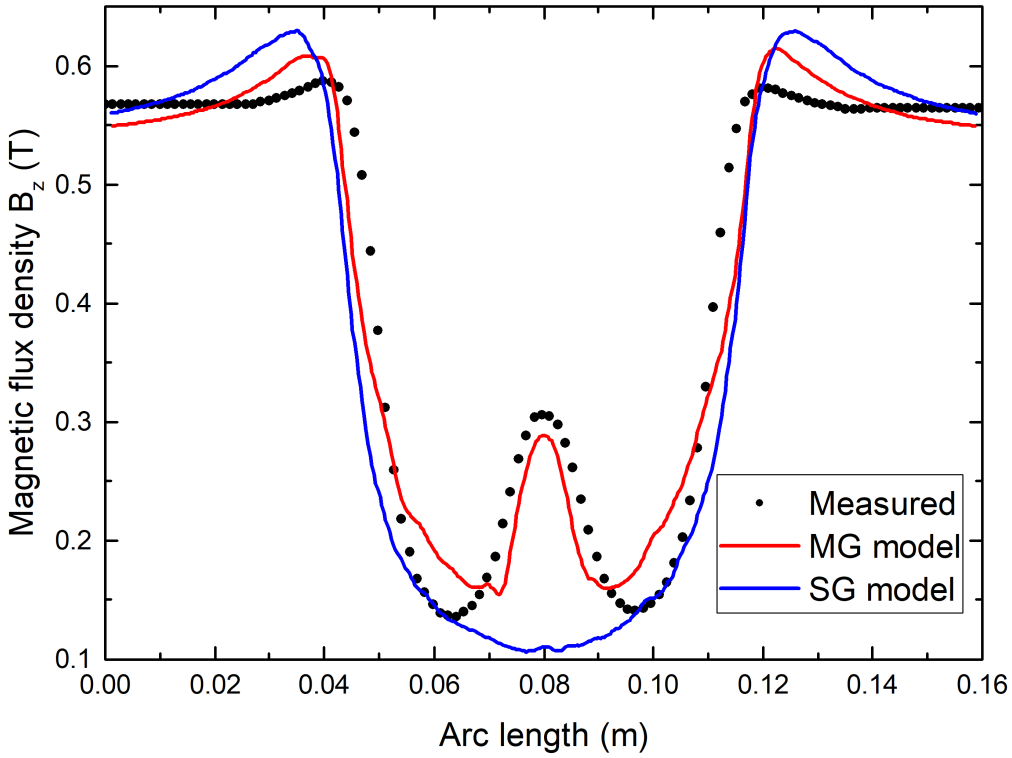

Figure 10. Comparison of the flux modulation calculated by the Single-Grain model (SG) and the Multi-Grain model (MG) with the measured flux modulation in the prototype for an applied magnetic flux density of 0.55 T.

The MG model can be used to extrapolate the multi-seeded bulk behavior for higher applied magnetic fields. Therefore, Figure 11 shows the B_1 value calculated with the MG and SG models for different magnetic fields applied by the coil. With an external field of 0.2 T, there is no difference between the use of a multi-seeded and single-seeded bulk. However, with an external field of 2 T, the machine torque is almost reduced by a factor of 2 for the multi-seeded bulks. Consequently, the MSMG method offers a good solution to reduce the price and the manufacturing time of the superconducting screens but is not suitable for flux modulation machines with an high magnetic loading.

These results and Figure 3 highlight the necessity of having a very high critical current density even at relatively high magnetic field, and particularly at the edges of the superconducting bulk as screening currents are concentrated on the edges of the bulk and almost null inside. Therefore, an efficient modulation will be obtained by a bulk with a good homogeneity of the performances all along the circumference of the superconductor. The synthesis method used to prepare the sample play a crucial role here and must be

chosen wisely as high power machines have a large volume and consequently require large bulks to make their rotors.

Moreover, Figure 12 presents the different possibles inductors for radial and axial flux modulation machines. While some inductors require easily manufactured bulk shapes, such as cuboids or disks, the ideal shapes for axial flux and radial flux structures are ring segment and tile shapes, respectively, which are more difficult to produce. Indeed, not all production methods are suitable for the production of large samples with complex shapes.

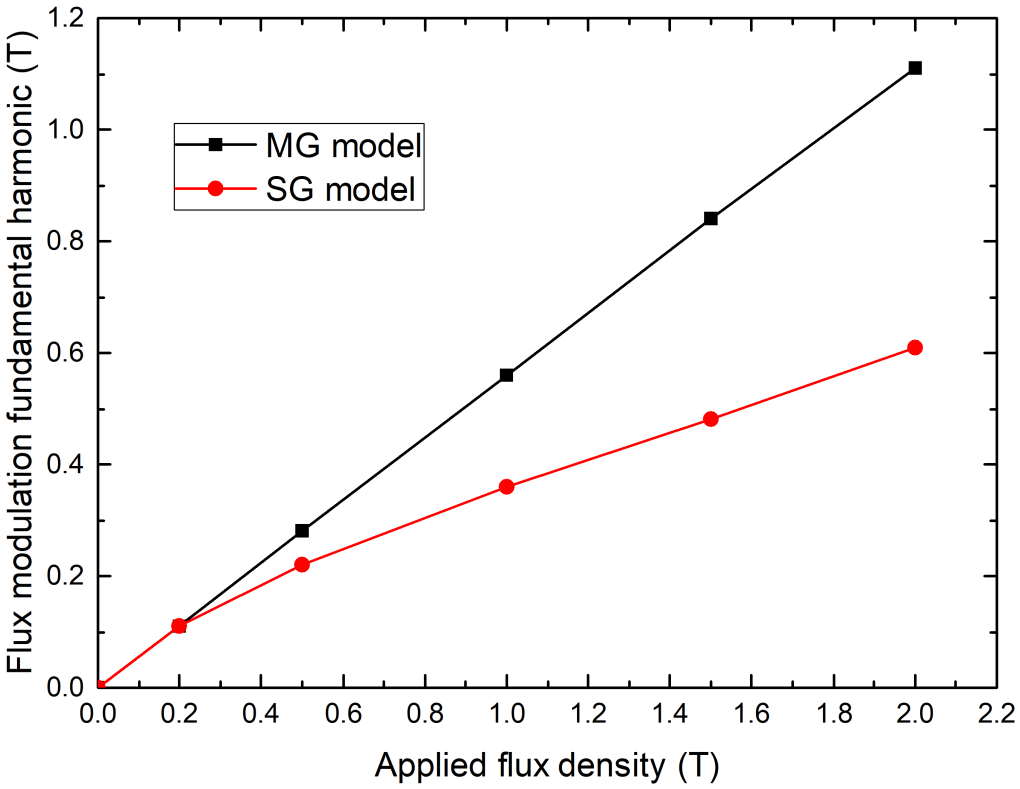

Figure 11. Simulated amplitude of the flux modulation fundamental harmonic in the air gap versus applied magnetic flux density for the SG and MG models.

Two major type of superconducting bulks can be synthesized: single crystal and poly-crystal. They are fundamentally different, as the single crystal can be seen as a single macroscopic grain with an homogeneous crystal orientation and a tiny number of structural defects, while a poly-crystal is made of multiple grains sintered together with a random crystal orientation and a large number of structural defect due to misalignment between grains, i.e., the grain boundary. This paper will be focused on the Top Seeded Melt Growth (TSMG) and the Infiltration growth (IG) synthesis techniques for single crystals as well as the classic sintering and the Spark Plasma Sintering (SPS) techniques for poly-crystals.

The TSMG method is widely known for the preparation of centimetric-scale single-crystal REBaCuO superconductors. Indeed, this technique is used for commercial bulks surperconductors [52,53] and shows a promising future as the synthesis size limit is regularly increasing [54]. Furthermore, the critical current density of such superconductors is really high and shows good mechanical properties. However, this technique is really time consuming as it requires 230 h for the crystal growth and 300 h of oxygen annealing for a standard 13 cm^3 cylinder of bulk GdBaCuO [55] and increase with the size of the sample. Furthermore, the presence of the so-called growth sector boundaries makes the homogeneity almost impossible to achieve as a misalignment is occurring along those boundaries [56]. Even more problematic is the evolution of the superconducting properties along the sample radius as reported in several papers [57–59]. For example, Antal et al. [45] present a diminuation of 24% of the J_c of two samples distant of only 8 mm along the

radius of a commercial YBaCuO bulk at 2 T and 4.2 K. Finally, for very large sample the homogeneity is even harder to achieve as it cannot be control during the preparation process, either during the synthesize or the machining, the consequence is the presence of weak parts where superconductivity is bad. This can be seen in Figure 13 where, for a large commercial ring segment-shaped GdBaCuO bulk, a weak area of superconductivity can be seen during a field cooling magnetization at 77 K.

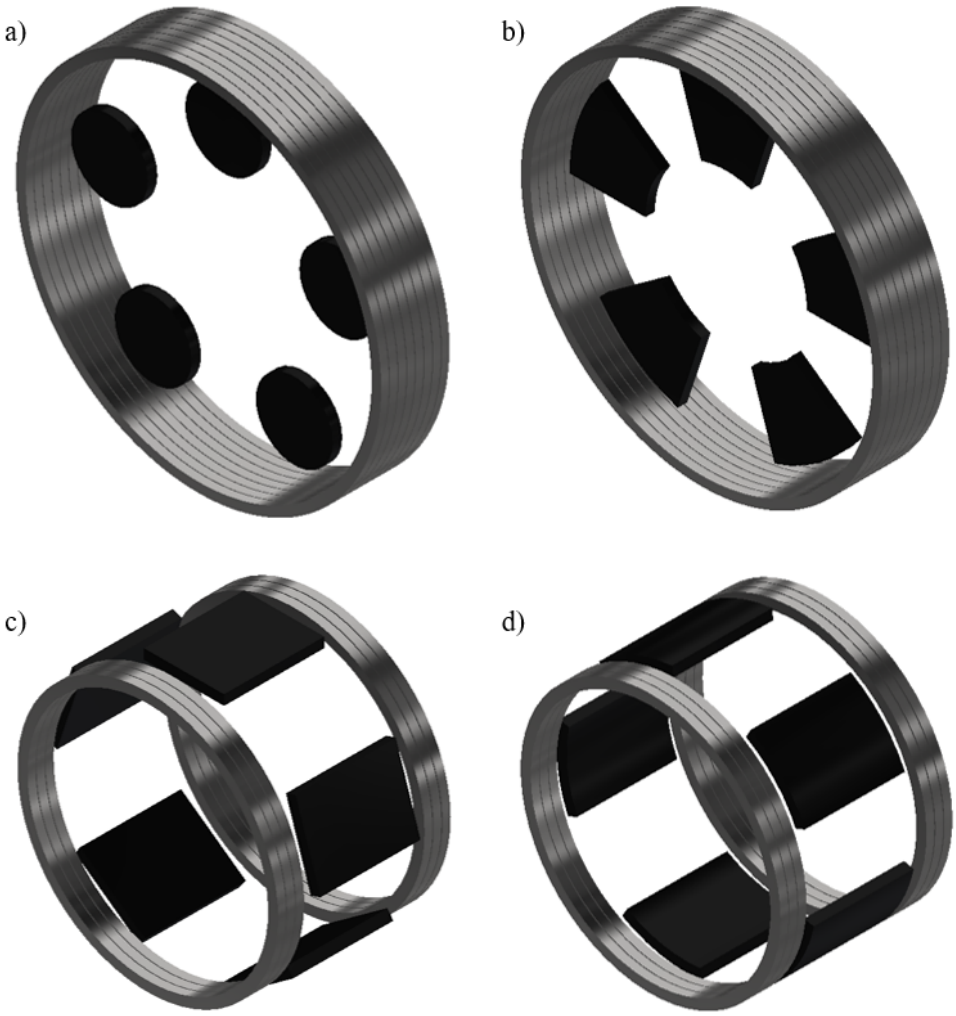

Figure 12. Representation of possible topologies of flux modulation inductors with the different bulk shapes. (**a**) Axial flux topology with disc-shaped bulks. (**b**) Axial flux topology with ring segment-shaped bulks. (**c**) Radial flux topology with cuboid-shaped bulks. (**d**) Radial flux topology with tile-shaped bulks.

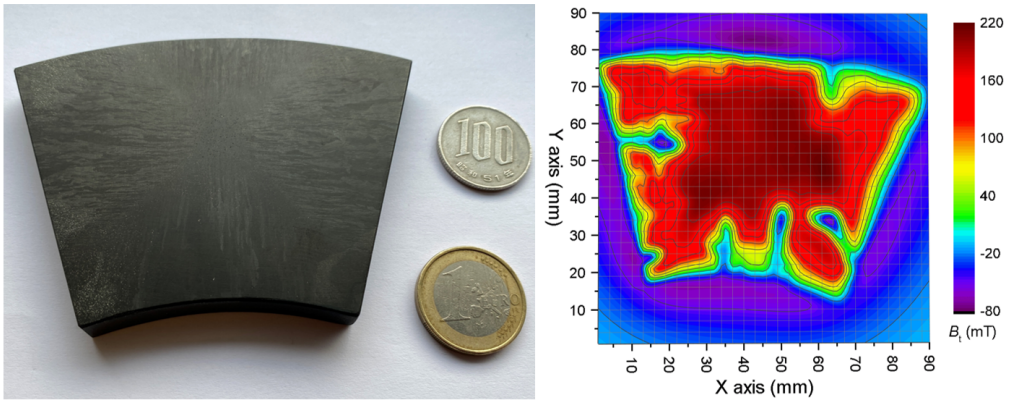

Figure 13. Left: Picture of a commercial ring segment shaped GdBaCuO bulk from can superconductors. **Right**: Corresponding measured trapped field map B_t of the bulk magnetized by field cooling with a permanent magnet in liquid nitrogen at 77 K.

Another method for preparing large size single crystal is the so-called infiltration-growth technique. This method requires a matrix of precursor materials, a liquid reactive material, and like for the TSMG, a seed on the top of the bulk [60–62]. Contrary to the TSMG method, it is easy to control the shape and the density of the precursor matrix and so the characteristics of the prepared superconducting bulk. As an example, by using a very porous starting material, it is even possible to prepare a foam-like sample [63–65]. However, this method processes the same drawbacks as TSMG which are a long synthesis time as well as a difficulty for preparing very large samples.

Toward the synthesis of large scale REBaCuO with several seeds, an improvement of the grain boundary superconducting properties can be obtained through superconducting welding technique. The welding of YBaCuO bulks requires a solder material with a low peritectic temperature such as REBaCuO with an heavy rare earth, e.g., Yb, Er [66–71], or a YBaCuO with a dopant reducing its peritectic temperature such as Ag [72–74]. This method has been shown to be more effective than MSMG [75], while being very fast to realize compared to the time required for the TSMG [76,77]. Figure 14 shows a 10 mm × 10 mm × 7.5 mm GdBaCuO+Ag sample with a ErBaCuO+Ag weld at the middle and its trapped magnetic field map in liquid nitrogen (LN_2). The weld was realized along the (110/110) plane with 12 h of crystal growth and 48 h of oxygen annealing. It can be seen on the field map that the welding has no impact on the trapped field showing a good connection between the two soldered parts. However, welding is a process that remains difficult to perform for large samples.

In the other side, poly-crystalline bulks are widely prepared by sintering, a very quick, simple, and cheap method [41,50,78]. This also allow the preparation of very large samples scale, tens of centimeters or even more, and with a totally free shape. However, it is hard to guarantee a good homogeneity of the temperature inside the furnace or a good powder mix during the synthesis or the annealing process. This lack of control and precision may induces the apparition of secondary phases with potentially other magnetic properties which lowers the sample performance [78,79]. Furthermore, a poly-crystal shows problematic grain boundaries, due to misorientation, the presence of defects, impurities, and a low density. The consequence is a low connectivity and so a low critical current as well as poor mechanical properties. Furthermore, this random orientation vanishes the macroscopic anisotropy of the crystal by averaging the local anisotropy of all grains.

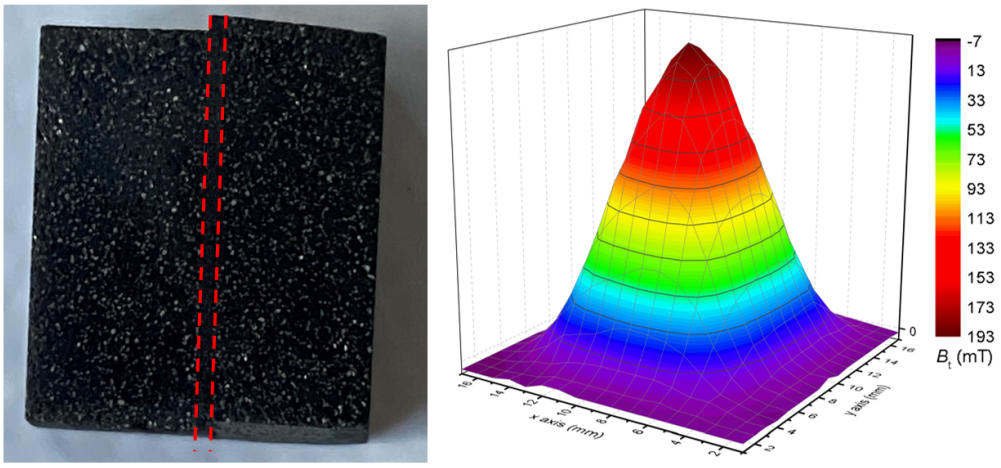

Figure 14. Left: Picture of a GdBaCuO commercial bulk produced by Nippon Steel. It has been cut and then welded with an ErBaCuO+Ag welding delimited by the dashed lines. **Right**: Corresponding measured trapped field map B_t of the welded bulk magnetized by field cooling with a permanent magnet in liquid nitrogen at 77 K.

One way to dramatically improve the performance of a polycrystaline sample is the use of the so-called Spark Plasma Sintering (SPS). It consists of increase the sample temperature by joule effect, a current is applied though the sample to reach very quickly the target temperature with a very good homogeneity all along the sample. At the same time the sample is pressed between the current lead with the same order of pressure than used for the Hot Pressing technique, whereas hours are needed for sintering a sample using a furnace, only tens of minutes to an hour are needed using the SPS technique. Furthermore, the resulting sample has a very high density, easily above 80% of the theoretical density [31,41] or even above 95% [80], a very good grain connectivity, and a very good homogeneity. The consequence is a huge improvement of the critical current and the mechanical properties to reach a level closed to the one of a single crystal with only a tiny fraction of the preparation time.

4. Conclusions

We have seen that different superconducting materials are suitable for flux modulation machine. However, it is clear that the properties of ReBaCuO are superior to its counterparts, especially in terms of high field critical current and critical temperature, thus allowing to reach better performances. Nevertheless, the synthesis of large size and homogeneous REBaCuO bulks is difficult and time-consuming despite the different techniques that could be employed to overcome these issues. Therefore, it might be appropriate to consider other materials such as MgB_2 or something iron-based as an alternative. Indeed, those materials have reasonable properties and their production requires only sintering which allows to rapidly and cost-effectively produce large sized and complex shaped bulk at low cost compared to REBaCuO.

Moreover, much progress can be achieved through doping and SPS processes to reach similar screening capacities to the REBaCuO for magnetic fields below 2 T which would already generate a large magnetic loading in an electrical machine. In addition, KFeSe, MgB_2, and several Pnitides (such as CaKFeAs) do not include any rare earth material unlike REBaCuO, which is of important environmental, political, and economical concern.

Author Contributions: Conceptualization, R.D. and Q.N.; Data curation, R.D., Q.N. and A.C.; Formal analysis, R.D., Q.N. and A.C.; Funding acquisition, R.D. and Q.N.; Investigation, R.D., Q.N., K.B. and K.S.; Methodology, R.D. and Q.N.; Project administration, R.D. and Q.N.; Resources, R.D., Q.N. and A.C.; Software, R.D., Q.N. and A.C.; Supervision and validation, all authors; Visualization, R.D. and Q.N.; Writing—original draft, R.D. and Q.N.; Writing—review & editing, R.D., Q.N. and K.B. All authors have read and agreed to the published version of the manuscript.

Funding: This research was founded by the international project SUPERFOAM ANR-17-CE05-0030 and DFG-Ko2323-10, the FROST project ANR-19-ASMA-0001, the AID, the Carnot ICEEL and the Carnot EnergICs.

Institutional Review Board Statement: Not applicable.

Informed Consent Statement: Not applicable.

Data Availability Statement: Data are contained within the article.

Acknowledgments: This work is part of the SUPERFOAM international project funded by ANR and DFG under the references ANR-17-CE05-0030 and DFG-ANR Ko2323-10, respectively. The authors would like to thank the Direction Générale de l'Armement (DGA), the Agence de l'Innovation de Défense (AID) and the Agence Nationale de la Recherche (ANR), FROST project, reference ANR-19-ASMA-0001, for the support and funding of this work. The authors would also like to acknowledge the Carnot ICEEL and the Carnot EnergICs cluster for the financial support of this work.

Conflicts of Interest: The authors declare no conflicts of interest.

References

1. Haran, K.S.; Loder, D.; Deppen, T.O.; Zheng, L. Actively shielded high-field air-core superconducting machines. *IEEE Trans. Appl. Supercond.* **2016**, *26*, 98–105. [CrossRef]
2. Huang, Z.; Zhang, M.; Wang, W.; Coombs, T.A. Trial test of a bulk-type fully HTS synchronous motor. *IEEE Trans. Appl. Supercond.* **2013**, *24*, 4602605.
3. Manolopoulos, C.D.; Iacchetti, M.F.; Smith, A.C.; Berger, K.; Husband, M.; Miller, P. Stator Design and Performance of Superconducting Motors for Aerospace Electric Propulsion Systems. *IEEE Trans. Appl. Supercond.* **2018**, *28*, 5207005. [CrossRef]
4. Yazdani-Asrami, M.; Zhang, M.; Yuan, W. Challenges for developing high temperature superconducting ring magnets for rotating electric machine applications in future electric aircrafts. *J. Magn. Magn. Mat.* **2021**, *522*, 167543. [CrossRef]
5. Douine, B.; Berger, K.; Ivanov, N. Characterization of High-Temperature Superconductor Bulks for Electrical Machine Application. *Materials* **2021**, *14*, 1636. [CrossRef] [PubMed]
6. Fukuda, S.; Yun, K.; Iwakuma, M.; Miura, S.; Sato, S.; Yoshida, K.; Tomioka, A.; Konno, M.; Izumi, T. Design Study of 2-MW Fully Superconducting Synchronous Motors. *IEEE Trans. Appl. Supercond.* **2018**, *28*, 5207806. [CrossRef]
7. Weng, F.; Zhang, M.; Lan, T.; Wang, Y.; Yuan, W. Fully superconducting machine for electric aircraft propulsion: Study of AC loss for HTS stator. *Supercond. Sci. Technol.* **2020**, *33*, 104002. [CrossRef]
8. Torrey, D.; Parizh, M.; Bray, J.; Stautner, W.; Tapadia, N.; Xu, M.; Wu, A.; Zierer, J. Superconducting Synchronous Motors for Electric Ship Propulsion. *IEEE Trans. Appl. Supercond.* **2020**, *30*, 5204708. [CrossRef]
9. Haran, K.S.; Kalsi, S.; Arndt, T.; Karmaker, H.; Badcock, R.; Buckley, B.; Haugan, T.; Izumi, M.; Loder, D.; Bray, J.W.; et al. High Power Density Superconducting Rotating Machines—Development Status and Technology Roadmap. *Supercond. Sci. Technol.* **2017**, *30*, 123002. [CrossRef]
10. Masson, P.J.; Luongo, C.A. High power density superconducting motor for all-electric aircraft propulsion. *IEEE Trans. Appl. Supercond.* **2005**, *15*, 2226–2229. [CrossRef]
11. Boll, M.; Corduan, M.; Biser, S.; Filipenko, M.; Pham, Q.H.; Schlachter, S.; Rostek, P.; Noe, M. A Holistic System Approach for Short Range Passenger Aircraft with Cryogenic Propulsion System. *Supercond. Sci. Technol.* **2020**, *33*, 044014. [CrossRef]
12. Wang, H.; Deng, Z.; Ma, S.; Sun, R.; Li, H.; Li, J. Dynamic simulation of the HTS maglev vehicle-bridge coupled system based on levitation force experiment. *IEEE Trans. Appl. Supercond.* **2019**, *29*, 1–6. [CrossRef]
13. National Academies of Sciences, Engineering, and Medicine. *Commercial Aircraft Propulsion and Energy Systems Research: Reducing Global Carbon Emissions*; National Academies Press: Washington, DC, USA, 2016.
14. Golovanov, D.; Gerada, D.; Sala, G.; Degano, M.; Trentin, A.; Connor, P.H.; Xu, Z.; La Rocca, A.; Galassini, A.; Tarisciotti, L.; et al. 4MW Class High Power Density Generator for Future Hybrid-Electric Aircraft. *IEEE Trans. Transp. Electrif.* **2021**. [CrossRef]
15. Filipenko, M.; Kühn, L.; Gleixner, T.; Thummet, M.; Lessmann, M.; Möller, D.; Böhm, M.; Schröter, A.; Häse, K.; Grundmann, J.; et al. Concept Design of a High Power Superconducting Generator for Future Hybrid-Electric Aircraft. *Supercond. Sci. Technol.* **2020**, *33*, 054002. [CrossRef]
16. Corduan, M.; Boll, M.; Bause, R.; Oomen, M.P.; Filipenko, M.; Noe, M. Topology comparison of superconducting ac machines for hybrid electric aircraft. *IEEE Trans. Appl. Supercond.* **2020**, *30*, 5200810. [CrossRef]

17. Matsuzaki, H.; Kimura, Y.; Ohtani, I.; Izumi, M.; Ida, T.; Akita, Y.; Sugimoto, H.; Miki, M.; Kitano, M. An Axial Gap-Type HTS Bulk Synchronous Motor Excited by Pulsed-Field Magnetization with Vortex-Type Armature Copper Windings. *IEEE Trans. Appl. Supercond.* **2005**, *15*, 2222–2225. [CrossRef]
18. Grilli, F.; Benkel, T.; Hänisch, J.; Lao, M.; Reis, T.; Berberich, E.; Wolfstädter, S.; Schneider, C.; Miller, P.; Palmer, C.; et al. Superconducting Motors for Aircraft Propulsion: The Advanced Superconducting Motor Experimental Demonstrator Project. *J. Phys. Conf. Ser.* **2020**, *1590*, 012051. [CrossRef]
19. Malé, G.; Lubin, T.; Mezani, S.; Lévêque, J. Analytical calculation of the flux density distribution in a superconducting reluctance machine with HTS bulks rotor. *Math. Comput. Simul.* **2013**, *90*, 230–243. [CrossRef]
20. Masson, P.J.; Breschi, M.; Tixador, P.; Luongo, C.A. Design of HTS axial flux motor for aircraft propulsion. *IEEE Trans. Appl. Supercond.* **2007**, *17*, 1533–1536. [CrossRef]
21. Masson, P.J.; Pienkos, J.E.; Luongo, C.A. Scaling up of HTS motor based on trapped flux and flux concentration for large aircraft propulsion. *IEEE Trans. Appl. Supercond.* **2007**, *17*, 1579–1582. [CrossRef]
22. Colle, A.; Lubin, T.; Ayat, S.; Gosselin, O.; Lévêque, J. Analytical Model for the Magnetic Field Distribution in a Flux Modulation Superconducting Machine. *IEEE Trans. Mag.* **2019**, *55*, 8107309. [CrossRef]
23. Colle, A.; Lubin, T.; Ayat, S.; Gosselin, O.; Lévêque, J. Test of a Flux Modulation Superconducting Machine for Aircraft. *J. Phys. Conf. Ser.* **2020**, *1590*, 012052. [CrossRef]
24. Filipenko, M.; Biser, S.; Boll, M.; Corduan, M.; Noe, M.; Rostek, P. Comparative analysis and optimization of technical and weight parameters of turbo-electric propulsion systems. *Aerospace* **2020**, *7*, 107. [CrossRef]
25. Hsu, F.C.; Luo, J.Y.; Yeh, K.W.; Chen, T.K.; Huang, T.W.; Wu, P.M.; Lee, Y.C.; Huang, Y.L.; Chu, Y.Y.; Yan, D.; et al. Superconductivity in the PbO-type structure α-FeSe. *Proc. Natl. Acad. Sci. USA* **2008**, *105*, 14262–14264. [CrossRef] [PubMed]
26. Johnston, D.C. The Puzzle of High Temperature Superconductivity in Layered Iron Pnictides and Chalcogenides. *Adv. Phys.* **2010**, *59*, 803–1061. [CrossRef]
27. Paglione, J.; Greene, R.L. High-Temperature Superconductivity in Iron-Based Materials. *Nat. Phys.* **2010**, *6*, 645–658. [CrossRef]
28. Stewart, G.R. Superconductivity in Iron Compounds. *Rev. Mod. Phys.* **2011**, *83*, 1589–1652. [CrossRef]
29. Jin, S.; Wu, X.; Huang, Q.; Wu, H.; Ying, T.; Fan, X.; Sun, R.; Zhao, L.; Chen, X. Two New Parent Compounds for FeSe-Based Superconducting Phases. *arXiv* **2016**, arXiv:1607.01103.
30. Ying, T.P.; Chen, X.L.; Wang, G.; Jin, S.F.; Zhou, T.T.; Lai, X.F.; Zhang, H.; Wang, W.Y. Observation of Superconductivity at 30 46K in $A_xFe_2Se_2$ (A = Li, Na, Ba, Sr, Ca, Yb and Eu). *Sci. Rep.* **2012**, *2*, 426. [CrossRef]
31. Wu, G.; Xie, Y.L.; Chen, H.; Zhong, M.; Liu, R.H.; Shi, B.C.; Li, Q.J.; Wang, X.F.; Wu, T.; Yan, Y.J.; et al. Superconductivity at 56 K in Samarium-Doped SrFeAsF. *J. Phys. Condens. Matter* **2009**, *21*, 142203. [CrossRef]
32. Tarantini, C.; Gurevich, A.; Jaroszynski, J.; Balakirev, F.; Bellingeri, E.; Pallecchi, I.; Ferdeghini, C.; Shen, B.; Wen, H.H.; Larbalestier, D.C. Significant Enhancement of Upper Critical Fields by Doping and Strain in Iron-Based Superconductors. *Phys. Rev. B* **2011**, *84*, 184522. [CrossRef]
33. Ozaki, T.; Takeya, H.; Okazaki, H.; Deguchi, K.; Demura, S.; Kawasaki, Y.; Hara, H.; Watanabe, T.; Yamaguchi, T.; Takano, Y. One-Step Synthesis of $K_xFe_2Se_2$ Single Crystal for High Critical Current Density. *EPL* **2012**, *98*, 27002. [CrossRef]
34. Murakami, M.; Sakai, N.; Higuchi, T.; Yoo, S.I. Melt-processed light rare earth element-Ba-Cu-O. *Supercond. Sci. Technol.* **1996**, *9*, 1015–1032. [CrossRef]
35. Murakami, M. Processing of bulk YBaCuO. *Supercond. Sci. Technol.* **1992**, *5*, 185. [CrossRef]
36. Nariki, S.; Sakai, N.; Murakami, M. Melt-processed Gd-Ba-Cu-O superconductor with trapped field of 3 T at 77 K. *Supercond. Sci. Technol.* **2004**, *18*, S126. [CrossRef]
37. Tomita, M.; Murakami, M.; Tomita, M.; Murakami, M. High-temperature superconductor bulk magnets that can trap magnetic fields of over 17 tesla at 29 K. *Nature* **2003**, *421*, 517–520. [CrossRef]
38. Durrell, J.H.; Dennis, A.R.; Jaroszynski, J.; Ainslie, M.D.; Palmer, K.G.; Shi, Y.H.; Campbell, A.M.; Hull, J.; Strasik, M.; Hellstrom, E.E.; et al. A trapped field of 17.6 T in melt-processed, bulk Gd-Ba-Cu-O reinforced with shrink-fit steel. *Supercond. Sci. Technol.* **2014**, *27*, 082001. [CrossRef]
39. Nagamatsu, J.; Nakagawa, N.; Muranaka, T.; Zenitani, Y.; Akimitsu, J. Superconductivity at 39 K in Magnesium Diboride. *Nature* **2001**, *410*, 63–64. [CrossRef]
40. Kumakura, H.; Takano, Y.; Fujii, H.; Togano, K.; Kito, H.; Ihara, H. Critical current densities and irreversibility fields of MgB2 bulks. *Phys. C Supercond.* **2001**, *363*, 179–183. [CrossRef]
41. Noudem, J.G.; Xing, Y.; Bernstein, P.; Retoux, R.; Higuchi, M.; Arvapalli, S.; Muralidhar, M.; Murakami, M. Improvement of critical current density of MgB_2 bulk superconductor processed by Spark Plasma Sintering. *J. Am. Ceram Soc.* **2020**, *103*, 6169–6175. [CrossRef]
42. Badica, P.; Aldica, G.; Grigoroscuta, M.A.; Burdusel, M.; Pasuk, I.; Batalu, D.; Berger, K.; Koblischka-Veneva, A.; Koblischka, M.R. Reproducibility of Small $Ge_2C_6H_{10}O_7$-Added MgB_2 Bulks Fabricated by Ex Situ Spark Plasma Sintering Used in Compound Bulk Magnets with a Trapped Magnetic Field above 5 T. *Sci. Rep.* **2020**, *10*, 10538. [CrossRef]
43. Berger, K.; Koblischka, M.R.; Douine, B.; Noudem, J.; Bernstein, P.; Hauet, T.; Lévêque, J. High magnetic field generated by bulk MgB 2 prepared by spark plasma sintering. *IEEE Trans. Appl. Supercond.* **2016**, *26*, 6801005. [CrossRef]
44. Berger, K.; Lévêque, J.; Netter, D.; Douine, B.; Rezzoug, A. Influence of Temperature and/or Field Dependences of the $E - J$ Power Law on Trapped Magnetic Field in Bulk YBaCuO. *IEEE Trans. Appl. Supercond.* **2007**, *17*, 3028–3031. [CrossRef]

45. Antal, V.; Zmorayová, K.; Rajňak, M.; Vojtkova, L.; Hlásek, T.; Plecháček, J.; Diko, P. Relationship between local microstructure and superconducting properties of commercial YBa2Cu3O7-δbulk. *Supercond. Sci. Technol.* **2020**, *33*, 044004. [CrossRef]
46. van Dalen, A.J.J.; Koblischka, M.R.; Griessen, R.; Jirsa, M.; Ravi Kumar, G. Dynamic Contribution to the Fishtail Effect in a Twin-Free DyBa2Cu3O7-δ Single Crystal. *Phys. C Supercond.* **1995**, *250*, 265–274. [CrossRef]
47. Yang, H.; Luo, H.; Wang, Z.; Wen, H.-H. Fishtail Effect and the Vortex Phase Diagram of Single Crystal Ba0.6K0.4Fe2As2. *Appl. Phys. Lett.* **2008**, *93*, 142506. [CrossRef]
48. Luo, H.; Wang, Z.; Yang, H.; Cheng, P.; Zhu, X.; Wen, H.H. Growth and characterization of A_1− xK_xFe2As2 (A= Ba, Sr) single crystals with x= 0–0.4. *Supercond. Sci. Technol.* **2008**, *21*, 125014. [CrossRef]
49. Guilmeau, E.; Noudem, J. Influence of the sinter-forging temperature on the superconducting properties of Bi2223 textured discs. *Supercond. Sci. Technol.* **2002**, *15*, 1566. [CrossRef]
50. Ishida, S.; Pavan Kumar Naik, S.; Tsuchiya, Y.; Mawatari, Y.; Yoshida, Y.; Iyo, A.; Eisaki, H.; Kamiya, Y.; Kawashima, K.; Ogino, H. Synthesis of CaKFe4As4 bulk samples with high critical current density using a spark plasma sintering technique Supercond. *Sci. Technol.* **2020**, *33*, 094005.
51. Werfel, F.N.; Floegel-Delor, U.; Riedel, T.; Goebel, B.; Rothfeld, R.; Schirrmeister, P.; Wippich, D. Large-scale HTS bulks for magnetic application. *Phys. C Supercond.* **2013**, *484*, 6–11. [CrossRef]
52. Hlásek, T.; Plecháček, V. Long-Term Quality Observation in Large-Scale Production of Top-Seeded Melt Growth YBCO Bulks. *IEEE Trans. Appl. Supercond.* **2017**, *27*, 6801004. [CrossRef]
53. Werfel, F.N.; Floegel-Delor, U.; Rothfeld, R.; Riedel, T.; Goebel, B.; Wippich, D.; Schirrmeister, P. Superconductor Bearings, Flywheels and Transportation. *Supercond. Sci. Technol.* **2011**, *25*, 014007. [CrossRef]
54. Sakai, N.; Kita, M.; Nariki, S.; Muralidhar, M.; Inoue, K.; Hirabayashi, I.; Murakami, M. Field trapping property of Gd–Ba–Cu–O bulk superconductor 140 mm in diameter. *Phys. C Supercond. Its Appl.* **2006**, *445*, 339–342. [CrossRef]
55. Shi, Y.; Babu, N.H.; Iida, K.; Yeoh, W.K.; Dennis, A.R.; Pathak, S.K.; Cardwell, D.A. Batch-processed GdBCO–Ag bulk superconductors fabricated using generic seeds with high trapped fields. *Phys. C Supercond. Its Appl.* **2010**, *470*, 685–688. [CrossRef]
56. Ainslie, M.D.; Fujishiro, H.; Ujiie, T.; Zou, J.; Dennis, A.R.; Shi, Y.H.; Cardwell, D.A. Modelling and comparison of trapped fields in (RE) BCO bulk superconductors for activation using pulsed field magnetization. *Supercond. Sci. Technol.* **2014**, *27*, 065008. [CrossRef]
57. Shi, Y.; Gough, M.; Dennis, A.R.; Durrell, J.H.; Cardwell, D.A. Distribution of the superconducting critical current density within a Gd–Ba–Cu–O single grain. *Supercond. Sci. Technol.* **2020**, *33*, 044009. [CrossRef]
58. Hlásek, T.; Shi, Y.; Durrell, J.H.; Dennis, A.R.; Namburi, D.K.; Plecháček, V.; Rubešová, K.; Cardwell, D.A.; Jankovský, O. Cost-Effective Isothermal Top-Seeded Melt-Growth of Single-Domain YBCO Superconducting Ceramics. *Solid State Sci.* **2019**, *88*, 74–80. [CrossRef]
59. Eisterer, M.; Haindl, S.; Zehetmayer, M.; Gonzalez-Arrabal, R.; Weber, H.W.; Litzkendorf, D.; Zeisberger, M.; Habisreuther, T.; Gawalek, W.; Shlyk, L. Limitations for the trapped field in large grain YBCO superconductors. *Supercond. Sci. Technol.* **2006**, *19*, S530. [CrossRef]
60. Pavan Kumar Naik, S.; Muralidhar, M.; Jirsa, M.; Murakami, M. Growth and Physical Properties of Top-Seeded Infiltration Growth Processed Large Grain (Gd, Dy)BCO Bulk Superconductors. *J. Appl. Phys.* **2017**, *122*, 193902. [CrossRef]
61. Pavan Kumar Naik, S.; Miryala, M.; Koblischka, M.R.; Koblischka-Veneva, A.; Oka, T.; Murakami, M. Production of Sharp-Edged and Surface-Damaged Y_2BaCuO_5 by Ultrasound: Significant Improvement of Superconducting Performance of Infiltration Growth-Processed $YBa_2Cu_3O_{7-\delta}$ Bulk Superconductors. *ACS Omega* **2020**, *5*, 6250–6259. [CrossRef]
62. Namburi, D.K.; Takahashi, K.; Hirano, T.; Kamada, T.; Fujishiro, H.; Shi, Y.-H.; Cardwell, D.A.; Durrell, J.H.; Ainslie, M.D. Pulsed-Field Magnetisation of Y-Ba-Cu-O Bulk Superconductors Fabricated by the Infiltration Growth Technique. *Supercond. Sci. Technol.* **2020**, *33*, 115012. [CrossRef]
63. Reddy, E.S.; Schmitz, G.J. Superconducting Foams. *Supercond. Sci. Technol.* **2002**, *15*, L21–L24. [CrossRef]
64. Koblischka, M.R.; Koblischka-Veneva, A.; Berger, K.; Nouailhetas, Q.; Douine, B.; Reddy, E.S.; Schmitz, G.J. Current Flow and Flux Pinning Properties of YBCO Foam Struts. *IEEE Trans. Appl. Supercond.* **2019**, *29*, 1–5. [CrossRef]
65. Koblischka, M.R.; Naik, S.P.K.; Koblischka-Veneva, A.; Murakami, M.; Gokhfeld, D.; Reddy, E.S.; Schmitz, G.J. Superconducting YBCO Foams as Trapped Field Magnets. *Materials* **2019**, *12*, 853. [CrossRef] [PubMed]
66. Mukhopadhyay, S.M.; Mahadev, N.; Sengupta, S. Microstructural and spectroscopic analyses of a strongly-linked joint formed in a superconductor. *Phys. C Supercond.* **2020**, *329*, 95–101. [CrossRef]
67. Noudem, J.G.; Reddy, E.S.; Tarka, M.; Noe, M.; Schmitz, G.J. Melt-texture joining of YBa2Cu3O y bulks. *Supercond. Sci. Technol.* **2001**, *14*, 363. [CrossRef]
68. Iida, K.; Yoshioka, J.; Sakai, N.; Murakami, M. Superconducting joint of Y–Ba–Cu–O superconductors using Er–Ba–Cu–O solder. *Phys. C Supercond.* **2002**, *370*, 53–58. [CrossRef]
69. Iida, K.; Yoshioka, J.; Negichi, T.; Noto, K.; Sakai, N.; Murakami, M. Strong coupled joint for Y–Ba–Cu–O superconductors using a sintered Er–Ba–Cu–O solder. *Phys. C Supercond.* **2002**, *378*, 622–626. [CrossRef]
70. Iida, K.; Yoshioka, J.; Sakai, N.; Murakami, M. Welding of different Y–Ba–Cu–O blocks. *Phys. C Supercond.* **2003**, *392*, 437–440. [CrossRef]
71. Yoshioka, J.; Iida, K.; Negichi, T.; Sakai, N.; Noto, K.; Murakami, M. Joining Y123 bulk superconductors using Yb–Ba–Cu–O and Er–Ba–Cu–O solders. *Supercond. Sci. Technol.* **2002**, *15*, 712. [CrossRef]

72. Harnois, C.; Desgardin, G.; Laffez, I.; Chaud, X.; Bourgault, D. High quality weld of melt textured YBCO using Ag doped YBCO junctions. *Phys. C Supercond.* **2002**, *383*, 269–278. [CrossRef]
73. Harnois, C.; Desgardin, G.; Chaud, X. A new way of welding $YBa_2Cu_3O_{7-\delta}$ bulk textured domains. *Supercond. Sci. Technol.* **2001**, *14*, 708. [CrossRef]
74. Hopfinger, T.; Viznichenko, R.; Krabbes, G.; Fuchs, G.; Nenkov, K. Joining of multi-seeded YBCO melt-textured samples using YBCO/Ag composites as welding material. *Phys. C Supercond.* **2003**, *398*, 95–106. [CrossRef]
75. Harnois, C.; Chaud, X.; Laffez, I.; Desgardin, G. Joining of YBCO textured domains: A comparison between the multi-seeding and the welding techniques. *Phys. C Supercond.* **2002**, *372*, 1103–1106. [CrossRef]
76. Wei, G.; Guisheng, Z.; Xiao, C.; Aiping, W.; Jiarun, H.; Hailin, B.; Jialie, R.; Yulei, J. Joining of Textured YBCO with YBCO Added Ag2O Additive. *Phys. C Supercond.* **2010**, *470*, 482–486. [CrossRef]
77. Chai, X.; Zou, G.; Guo, W.; Wu, A.; He, J.; Bai, H.; Xiao, L.; Jiao, Y.; Jialie, R. Fast Joining of Melt Textured Y–Ba–Cu–O Bulks with High Quality. *Phys. C Supercond.* **2010**, *470*, 598–601. [CrossRef]
78. Nouailhetas, Q.; Koblischka-Veneva, A.; Koblischka, M.R.; Naik S, P.K.; Schäfer, F.; Ogino, H.; Motz, C.; Berger, K.; Douine, B.; Slimani, Y.; et al. Magnetic Phases in Superconducting, Polycrystalline Bulk FeSe Samples. *AIP Adv.* **2021**, *11*, 015230. [CrossRef]
79. Galluzzi, A.; Polichetti, M.; Buchkov, K.; Nazarova, E.; Mancusi, D.; Pace, S. Evaluation of the Intragrain Critical Current Density in a Multidomain FeSe Crystal by Means of Dc Magnetic Measurements. *Supercond. Sci. Technol.* **2015**, *28*, 115005. [CrossRef]
80. Aldica, G.; Burdusel, M.; Popa, S.; Enculescua, M.; Pasuka, I.; Badica, P. The influence of heating rate on superconducting characteristics of MgB2 obtained by spark plasma sintering technique. *Phys. C* **2015**, *19*, 184–189. [CrossRef]